crystals

MDPI

Review

Advanced Scanning Probe Microscopy of Graphene and Other 2D Materials

Chiara Musumeci

Department of Materials Science and Engineering and NU*ANCE* Center, Northwestern University, Evanston, IL 60208, USA; chiara.musumeci@northwestern.edu

Academic Editor: Filippo Giannazzo
Received: 17 May 2017; Accepted: 7 July 2017; Published: 11 July 2017

Abstract: Two-dimensional (2D) materials, such as graphene and metal dichalcogenides, are an emerging class of materials, which hold the promise to enable next-generation electronics. Features such as average flake size, shape, concentration, and density of defects are among the most significant properties affecting these materials' functions. Because of the nanoscopic nature of these features, a tool performing morphological and functional characterization on this scale is required. Scanning Probe Microscopy (SPM) techniques offer the possibility to correlate morphology and structure with other significant properties, such as opto-electronic and mechanical properties, in a multilevel characterization at atomic- and nanoscale. This review gives an overview of the different SPM techniques used for the characterization of 2D materials. A basic introduction of the working principles of these methods is provided along with some of the most significant examples reported in the literature. Particular attention is given to those techniques where the scanning probe is not used as a simple imaging tool, but rather as a force sensor with very high sensitivity and resolution.

Keywords: scanning probe microscopy; 2D materials; opto-electronic properties; mechanical properties; nanoscale characterization

1. Introduction

The growing interest in atomically thin two-dimensional (2D) materials, driven by the continuous discovery of new properties and low-dimensional physics, provides fertile ground for revolutionary post-silicon electronics [1–3]. Graphene is the most studied among 2D materials [4] because of its high ambipolar mobility, unique band structure, and a wealth of interesting properties such as the presence of massless Dirac fermions, the room temperature quantum hall effect, quasiparticle symmetry, chirality, and pseudospin [5–9]. Other 2D materials, such as transition metal dichalcogenides (TMDs) [10], have practical applications and fundamental properties complementary to those of graphene [11]. They exhibit atomically sharp interfaces, ultrathin dimensions, flexibility, and large optical effects [12]. Molybdenum disulfide (MoS_2), for example, has been tested in proof-of-concept ultrafast field-effect transistors (FETs), optical devices, and flexible electronics [13–15]. The presence of a band gap in a 6.5 Å thin monolayer MoS_2 makes it suitable for applications in nanoelectronics, allowing for the fabrication of transistors with low power dissipation, high current on/off ratios, and high charge mobility. Various memory devices have been fabricated with 2D materials, showing low power and energy consumption [16] as well as the possibility to be integrated in flexible devices [17]. Memristors based on grain boundaries in single layer MoS_2 devices have shown switching ratios up to ~10^3 [18].

Because of its high resolution and its ability to correlate several properties with the sample morphology at nanoscale [19,20], scanning probe microscopy has given a vast and valuable contribution to the understanding of the fundamental properties of graphene and other 2D materials [21]. Despite being a single-atom thick sheet, graphene is not perfectly flat. Corrugations

up to 1 nm normal to the plane of the sheet, ripples, are commonly observed and thought to impart stability to the 2D lattice [22,23]. Only single-layer graphene is a zero-gap semiconductor, with one type of electron and one type of hole, while for three or more layers, several charge carriers appear and the conduction and valence bands start overlapping [7]. The aspect ratio of the graphene flakes influences the minimum conductivity [24]; and ripples also play a role in its electronic properties by inducing charge inhomogeneity as a consequence of the rehybridization of the π-σ bonding [23]. Large area films of 2D materials are polycrystalline. Consequently, grain boundaries, i.e., the interfaces between single-crystalline domains, inevitably affect their electronic transport, optical, mechanical, and thermal properties [25]. Optimizing large-scale growth processes for increasing the size of single-crystalline graphene is one of the main vectors of research. However, purposefully introducing and manipulating topological disorder is expected to become another important research objective to tailor 2D materials. Exceptional magnetic properties, for example, arise from the interplay of dislocation-induced localized states, doping, and locally unbalanced stoichiometry in grain boundaries in TMDs [26]. The number of layers, the size of the flakes, deformations, and the presence of defects or adsorbed molecules thus hugely affect these materials' properties, and because of the nanoscopic nature of these features, a tool addressing morphological and functional characterization on this scale is fundamental [27].

The aim of this review is to present an overview of different Scanning Probe Microscopy techniques used for the characterization of 2D materials (Figure 1), going from Scanning Tunneling Microscopy (STM) to Atomic Force Microscopy (AFM), and from Electrostatic Force Microscopy (EFM) and Kelvin Probe Force Microscopy (KPFM) to Conductive Atomic Force Microscopy (C-AFM) and Photoconductive Atomic Force Microscopy (PC-AFM). A basic introduction of the principles of operation and several among the most significant examples in the literature are shown. Particular attention is then given to those modes enabling an accurate control of the mechanical forces involved when an AFM tip is interacting with a 2D crystal sheet, where the AFM is not used as a simple imaging tool, but rather as a force sensor with very high sensitivity. In this respect, Force Spectroscopy modes, Friction Force Microscopy (FFM), and Piezoresponse Force Microscopy (PFM) are identified as very valuable tools to get quantitative information on single and multilayer 2D materials, ultimately enabling the tuning of their properties through strain engineering [28].

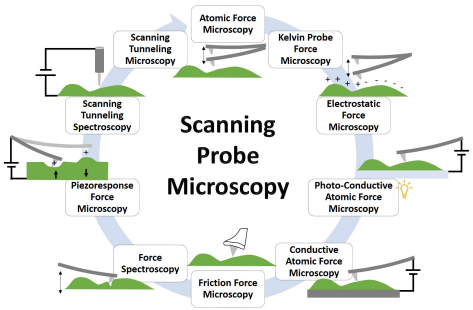

Figure 1. Scheme showing the different Scanning Probe Microscopy techniques described in this review for the characterization of two-dimensional (2D) materials.

2. Scanning Tunneling Microscopy

In a Scanning Tunneling Microscopy (STM) [29] experiment, a sharp metallic tip is separated by a few angstroms from a conductive sample. When a voltage is applied between the tip and the sample, electrons tunnel between them, producing an electric current, which decays exponentially with increasing tip–sample separation. In a standard operation, the current is kept constant during scanning by a feedback circuit, so that the vertical displacement of the scanner reflects the surface topography and gives true atomic resolution. Tip shape and sharpness are the two most important parameters in imaging surfaces, particularly those with significant topography. STM images invariably include contributions from specimen structure and tip geometry. Thus, the study of the tip's geometry

is indispensable in distinguishing between the apparent and the true structure, or to establish the relationship among the tip's geometry, the true surface structure, and the STM image [30–32].

The crystal lattice of single-layer graphene has been observed by STM measurements on a wide variety of substrates, such as SiO_2 [33–35], SiC [36,37], Ir [38], Pd [39], Cu [40], Ru(0001) [41], and h-BN [42], showing different degrees of corrugation (Figure 2a,b). Moreover, STM can also provide information about the density of states of the 2D samples by Scanning Tunneling Spectroscopy (STS) and differential conductance (dI/dV) measurements [43,44]. STS has allowed for the measurement of the Dirac point of graphene, and has been valuable in demonstrating the correlation between atomic structure, defects, and grain boundaries in the electronic properties of these single-layer crystals [45–47]. Figure 2c,d, for example, shows the energy position of the Dirac point, ED, as a function of applied gate voltage, which could be extracted from the conductance minimum in dI/dV measurements of graphene deposited on SiO_2 [34]. An STM tip has been recently used to strain a graphene sample locally, in the form of a small Gaussian bump, and at the same time to map the imbalance of the local density of states (LDOS) at the sublattice level, demonstrating the pseudospin polarization by a pseudomagnetic field [48].

The applications of 2D materials for thermal management and thermoelectric energy conversion is also an emerging field of investigation. Appropriate nanostructuring and bandgap engineering of graphene can strongly reduce the lattice thermal conductance and enhance the Seebeck coefficient without dramatically degrading the electronic conductance [49]. Atomic-scale mapping of the thermopower of epitaxial graphene has been performed using STM, revealing that the spatial distributions of thermovoltage have a direct correspondence to the electronic density of states, and local thermopower distortions result from the modification of the electronic structure induced by individual defects, such as wrinkles, at the monolayer-bilayer interfaces [50].

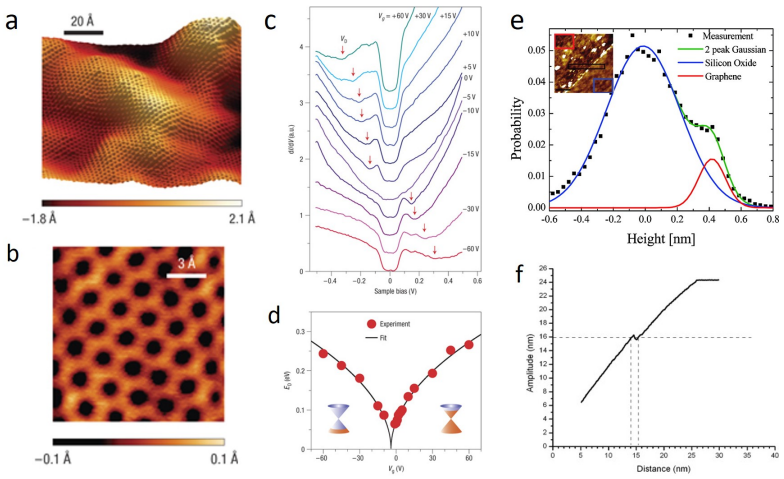

Figure 2. (**a**–**c**) Scanning Tunneling Microscopy (STM) of a graphene flake on a SiO_2 substrate. (**a**) Large scale constant current topography; (**b**) Close-up showing the honeycomb lattice; (**c**) dI/dV spectrum of graphene for different gate voltages, Vg, with red arrows indicating the gate-dependent positions of the conductance minimum outside the gap feature; (**d**) Energy position of the Dirac point, ED, as a function of applied gate voltage (extracted from the conductance minimum in (c) (adapted from [34]); (**e**) Height histogram acquired across the graphene-substrate boundary (see inset) of an Atomic Force Microscopy (AFM) image acquired in Non-Contact mode in ultrahigh vacuum (UHV). The data are fit by two Gaussian distributions with means separated by 4.2 Å (adapted from [35]); (**f**) The damping of the cantilever oscillation as a function of piezo displacement, recorded by approaching the tip towards the surface of a single graphene flake on silicon oxide substrate (adapted from [51]).

3. Atomic Force Microscopy

Atomic Force Microscopy images surfaces using the force exerted between the AFM probe and the sample as the feedback parameter [52]. To obtain an AFM topographic image, the sample is scanned

by a tip mounted on a cantilever spring. While scanning, a feedback loop maintains the force between the tip and the sample constant by adjusting pixel by pixel the scanner's height, so that the image is obtained by plotting the height position versus its position on the sample. There are different modes of operation, which differ for the nature of tip motion and tip–sample interaction. Interactions can be attractive or repulsive, ultimately setting the distance between the tip and the sample. In a static mode, i.e., *Contact* mode, the tip is raster scanned over the sample's surface by maintaining its deflection constant. In dynamic modes, such as *Tapping*, *Non-Contact*, and *PeakForce Tapping*, the tip oscillates and the feedback is given by the amplitude, frequency, or maximum force at the contact point.

The high resolution obtained with Non-Contact AFM has allowed the visualization of ultra-flat graphene monolayers deposited on mica. The apparent roughness in these graphene layers was less than 25 picometres over micrometer lateral length scales, indicating that intrinsic ripples can be strongly suppressed by interfacial van der Waals interactions when this material is supported on an appropriate atomically-flat substrate [35]. Despite the high resolution, which makes AFM able to visualize nanostructures and defects, such as induced nanoripples [53] and adsorbates [54] on graphene, some limitations are still present for the determination of the monolayer thickness.

Contact mode AFM has been used to determine the number of layers of graphene films, but differences in height have been observed between forward and reverse scans. These differences have been attributed to the high lateral forces, such as friction, which play a non-negligible role in influencing the cantilever bending, ultimately resulting in an inaccurate estimation of the thickness. Such forces are negligible in dynamic modes, which are therefore preferred over *Contact* mode [51]. However, a notable discrepancy in the values for a single-layer thickness measured by dynamic modes AFM is present in the literature, with values ranging from 0.3 to 1.7 nm for single-layer graphene [51,55–57] and from 0.6 to 1 nm for MoS_2 [13,58,59] being attributed to tip–surface interactions and the experimental environment (e.g., physisorbed water and impurities). Using *Non-contact* atomic force microscopy, Ishigami et al. measured the thickness of a graphene film in ultrahigh vacuum (UHV) and in ambient conditions, showing that the large height measured in ambient conditions is due to a significant presence of atmospheric species under and/or on the graphene film (Figure 2e) [35]. The most common mode used to image and measure the thickness of these layered materials is certainly *Tapping* mode (TM) AFM. Similarly to what generally occurs for nanostructure imaging [60], the optimization of the free amplitude of oscillation in tapping mode was shown to be critical to a correct single-layer thickness assessment. In this mode, long range attractive forces are responsible for the oscillation damping. When the tip starts to approach the sample, the amplitude decreases linearly. At a certain tip–sample separation, a jump occurs in the amplitude, marking the onset of a region where, upon decreasing the tip–sample distance further, both long range attractive forces and short range repulsive forces act on the tip (Figure 2f). By looking at the amplitude-displacement curves of single layer graphene, a jump could be indeed observed where two different piezo displacement values corresponded to the same amplitude, the difference being about 1 nm [51]. This implies that if the measurement setpoint is selected in such a way as to coincide with the jump in amplitude, the feedback electronics may produce random switching from one displacement value to the other. After the jump, the damping of the oscillation increases further, and net repulsive forces characterize the tip–sample interaction [61]. Nemes-Incze et al. showed that the amplitude of the tapping cantilever greatly influences the measured height of the very same graphene platelet, so that differences of as much as 1 nm could be observed. They also demonstrated that to gain reliable thickness data, one needs to use a setpoint where the tip scans in the net repulsive regime, where the damping of the cantilever is largely due to the topography of the sample [51]. Likewise, a reversible decrease of the measured height from 1.69 to 0.43 nm was observed when imaging in *PeakForce Tapping* with loading forces from 1 to 10 nN, with the true value being obtained at higher forces [62]. Significantly, the measured thickness of multilayer graphene flakes was found to be independent of the applied force, with a constant step of 0.3 nm. It was speculated that the water layer between the flakes and the substrate is squeezed when a higher force, that is higher pressure, is exerted on the single layer during imaging. This minimizes the artifact, and allows for a more

accurate measurement of the thickness. Both approaches, i.e., *Tapping* mode in a net repulsive regime and *PeakForce Tapping* at high contact forces, relying on the use of high forces during imaging, give a method to overcome the limitation of measuring single layers in ambient atmosphere, and therefore achieve a more accurate thickness measurement also in routine lab measurements.

Another fundamental issue is to image grain boundaries in 2D materials. Observing and engineering grain boundaries have been key in controlling the grain sizes, their electronic properties, and the related device performances. A valuable and easy method to observe grain boundaries rely on the combination of selective oxidation and AFM imaging. Selective oxidation is obtained by exposing directly the layers to ultraviolet light irradiation under moisture-rich conditions. The generated oxygen and hydroxyl radicals selectively functionalize defective grain boundaries, causing clear morphological changes at the boundaries, which can be clearly visualized by AFM imaging [63,64].

4. Electrical Modes

When AFM is operated in one of its electrical modes, it is possible to measure local electrical properties together with the sample's topography. These modes of operation make use of metal or metal-coated probes, and enable the application of an additional voltage between the tip and the sample. Electrostatic Force Microscopy (EFM) [65] and Kelvin Probe Force Microscopy (KPFM) [66] measures the contact potential difference or surface potential (SP) of a sample by recording long range electrostatic forces resulting from tip–sample interactions. These techniques provide a contactless electrical mapping of 2D flakes, allowing the extraction of crucial information about thickness, the distribution of the electrical potential and charge, as well as work function at nanoscale [20]. While the EFM method allows mainly for the qualitative mapping of surface potential, the KPFM technique provides quantitative values of the work function difference:

$$\Phi_s = \Phi_{tip} - eV_{CPD}, \quad (1)$$

where Φ_s and Φ_{tip} are the work functions of the sample and probe, respectively, and V_{CPD} is the contact potential difference directly measured by KPFM. In Conductive Atomic Force Microscopy (C-AFM) [67,68], the conductive tip acts as a movable electrode. The voltage is applied between the tip and a counter-electrode in contact with the sample, and a current is measured with high sensitivity, giving information on the local conductivity of the sample. In the simplest configuration, the sample is deposited on top of a conductive substrate and the conductive tip is scanned over such a surface by measuring point by point the current flowing vertically. Conversely, in a horizontal configuration, the sample is deposited on an insulating support and the electrical connection is obtained by laterally patterning a metal electrode. Current can in this way flow through the material, from the biased lateral contact to the movable metal-coated scanning probe tip [19]. In a similar configuration, named Photoconductive Atomic Force Microscopy (PC-AFM) [69], a light source is additionally used to excite the sample, so that the resulting photocurrent is measured by the AFM probe.

For electrical measurements, preventing probe-induced artifacts is very important. To obtain reliable data, the probe should be uniform, i.e., it should not have significant work function variations, and tip changes through tip–sample contact should be avoided. Optimal resolution in KPFM maps is obtained by long and slender but slightly blunt tips on cantilevers of minimal width and surface area [70]. However, tips modified with gold nanoparticles have also shown good resolution and sensitivity for graphene imaging [71]. Conductive tips fabricated by coating commercially available metal-varnished tips with graphene showed very high resistance to both high currents and frictions, leading to much longer lifetimes and preventing false imaging due to tip–sample interaction [72,73].

KPFM and EFM have been successfully used to identify the number of layers in epitaxial graphene [74]. Whereas an accurate topographical characterization is hindered by the presence of adsorbates in ambient conditions (see previous section), EFM can provide straightforward identification of the number of layers on the substrate [75]. Quantitative KPFM has revealed that graphene's work function is comparable to that of graphite, that is ~4.6 eV, and depends sensitively on the number of layers [76].

Theoretical studies have shown that the differences in surface potential between monolayers and bilayers can be ascribed to different substrate-induced doping levels [77]. Substrate characteristics, such as terrace width in SiC, can also be a dominating factor in determining the unintentional doping of monolayers [78]. Unique work function variations of graphene line defects, grain boundaries, standing-collapsed wrinkles, and folded wrinkles could be clearly identified by high-resolution KPFM (Figure 3a–c). Classical and quantum molecular dynamics simulations reveal that the work function distribution of each type of line defect is again originated from the doping effect induced by the substrate [79]. The abrupt change of the cantilever phase (fraction of phase shift >0.9, see Figure 3f) in the EFM images across a bisecting grain boundary (GB) in MoS_2 memory devices indicated that the electrostatic potential drops primarily at the grain boundary, i.e., the GB is resistive, consistently with the overall higher resistance of a bisecting-GB memristor compared to a bridge-GB memristor. Because the local surface potential and thus resistivity varies as a square root of the variation in the EFM phase signal, it was evaluated that more than 94% of the total device resistance would come from the grain boundary [18].

The doping caused by adsorbed molecules was also investigated by Pearce et al. [80], who showed a different sensitivity of monolayers and bilayers to chemical gating by exposing graphene samples to electron donating and withdrawing gases, and monitoring the change in work function via KPFM (Figure 3d,e). The larger shift in surface potential upon exposure to electron withdrawing and donating gases observed in monolayers rather than double layers was ascribed to the narrower energy dispersion around the Dirac point in graphene single sheets. The stepwise chemical reduction of individual graphene oxide flakes could be observed by monitoring the change of surface charge distribution, which revealed that the oxidized nanoscale domains are reduced by the leaching of sharp oxidized asperities from the surface followed by gradual thinning and the formation of uniformly mixed oxidized and graphitic domains across the entire flake [81]. Finally, electric field-induced changes in the work function of single layers were observed in gate modulated measurements, due to the Fermi level tuning induced by the gate voltage [82].

C-AFM has been successfully used to obtain spatial mapping of the conductivity of graphene on different substrates [83,84]. A high imaging contrast was used to distinguish domains of epitaxial graphene from the adjacent SiC surface thanks to strong differences in the tip–sample contact resistance [85]. The local conductance degradation in epitaxial graphene over the SiC substrate steps or at the junction between monolayer and bilayer regions could also be visualized, the degradation at the substrate steps being due to a lower substrate-induced electrostatic doping of graphene over the step sidewall, while that at the junction between the mono- and bilayer regions to the weak wave-function coupling between the monolayer and bilayer bands [86]. Also, by operating in current spectroscopy mode, i.e., by performing local I-V measurements, the Schottky barrier height (SBH) of epitaxial graphene grown on H-SiC was estimated to be 0.36 $\pm$ 0.1 eV, which is 0.49 eV lower than the barrier of graphene exfoliated from HOPG and deposited on the same substrate (0.85 $\pm$ 0.06 eV). The result was explained as a Fermi-level pinning effect above the Dirac point in epitaxial graphene due to the presence of positively charged states [87]. Similarly, C-AFM allowed the mapping of the spatial inhomogeneities of the SBH and the ideality factor of contacts on MoS_2, due to spatial variations in the density and energy of MoS_2 surface states, and to correlate local resistivity with local SBH [88]. Spatially resolved SBH maps revealed a substantial conductivity difference between MoS_2 with and without subsurface metal-like defects depending on the tip's work function, with high work function tips showing large spatial variations up to ~40% [89]. The nanoscale Schottky barrier distribution at the surface of multilayer MoS_2 could be tailored by varying the incorporated oxygen concentration by O_2 plasma functionalization. Whereas a narrow SBH distribution (0.2–0.3 eV) was measured for pristine MoS_2, a broader distribution (from 0.2 to 0.8 eV) in the modified one allowed both electrons and holes injection (Figure 4a–c) [90]. An attractive application of electrical mode SPMs is the use of conductive probes to induce electrochemical reactions and to pattern materials in electric field-induced nanolithography processes [91]. Local AFM-tip-induced electrochemical reduction processes were used to pattern conductive pathways on insulating graphene oxide to fabricate micropatterned graphene field-effect transistors featuring high charge-carrier mobilities

(Figure 4d,e) [92,93]. By changing the polarity of the applied voltage between graphene and a conductive AFM tip, hydrogenation and oxidation could be controlled at the nanoscale, and used to fabricate nanostructures such as graphene nanoribbons [94]. Changes due to the electro-reduction process could be monitored directly on a device by KPFM even at single sheet level [95].

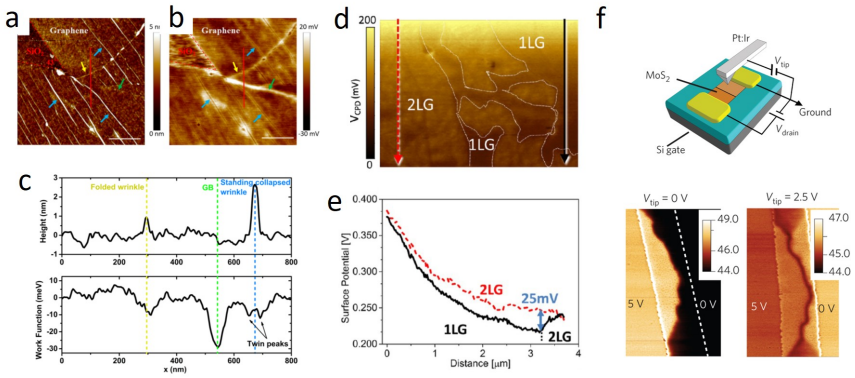

Figure 3. AFM topography (**a**) and Kelvin Probe Force Microscopy (KPFM) mapping (**b**) of standing collapsed wrinkles with various sizes; (**c**) Cross section profiles along the red line marked in (a) and (b). The dashed lines indicate the locations of folded wrinkle, grain boundaries, and standing collapsed wrinkle, respectively, with color coding corresponding to that in (a) and (b). Scale bars in (a) and (b) are 500 nm (adapted from [79]); (**d**) Surface potential map showing decreasing surface potential of single and double layer graphene with NO_2 exposure. The arrows represent the direction of the scan; (**e**) Section profiles along the arrows marked in (d) for single (black) and double (red) layer (adapted from [80]); (**f**) Device scheme and Electrostatic Force Microscopy (EFM) phase images of a bisecting grain boundary (GB) MoS_2 memristor at tip biases V_{tip} = 0 V and 2.5 V. Color scale bars show the EFM phase in degrees. Device bias conditions: V_{drain} = 5 V and V_{source} = V_g = 0 V. The dotted lines highlight the metal–MoS2 junctions with less contrast (adapted from [18]).

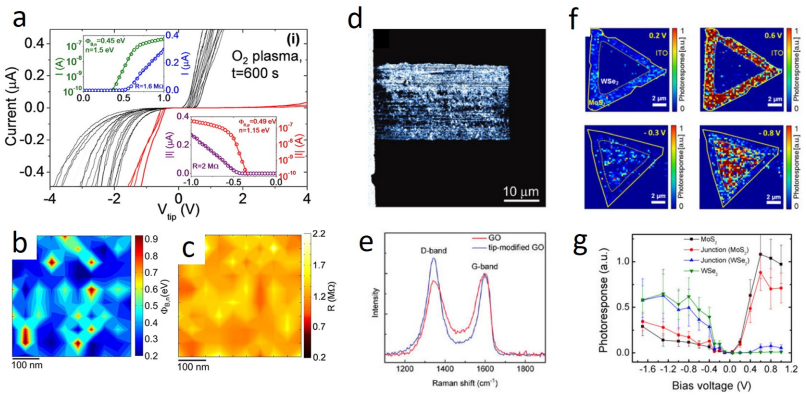

Figure 4. (**a**) Arrays of local current-voltage (I-V_{tip}) characteristics measured by Conductive Atomic Force Microscopy (C-AFM) on MoS2 subjected to O_2 plasma. Insets in (a) show fittings of representatives curves on linear- and semilog-scale to extract the local Schottky barrier height ($\Phi_{B,n}$) and the series resistance (R); (**b**,**c**) Two-dimensional (2D) maps of the local $\Phi_{B,n}$ and R (adapted from [90]); (**d**) C-AFM current map of a tip-modified rectangular region of a few-layer GO film with a top-contact gold electrode on the left side (current range 50 nA); (**e**) Raman spectra obtained on modified and unmodified GO (adapted from [92]); (**f**) Spatially resolved photoresponse maps and derived plot (**g**) of a WSe_2-MoS_2 heterostructure crystal in both forward (0.2 and 0.6 V) and reverse voltage (−0.3 V and −0.8 V) regimes under illumination of λ = 550 nm. The photoresponse maps are generated by subtracting a photocurrent map under illumination (Photoconductive Atomic Force Microscopy (PC-AFM) map) from a dark current map (C-AFM map), and normalized by the incident laser power at a selected wavelength. (adapted from [96]).

The combination of C-AFM and PC-AFM was demonstrated to be convenient and versatile to efficiently examine layer-dependent electronic and optoelectronic characteristics in 2D crystals containing regions of different thicknesses [97,98]. Current transport mechanisms and photoresponse of mono- and multilayers, as well as heterostructures, could be investigated at the nanoscale junctions. For example, in a fascinating experiment, Son et al. investigated WSe_2-MoS_2 heterostructures by C-AFM and PC-AFM. By modulating the polarity and magnitude of the applied voltage, the photoresponse could be selectively switched on and off in a portion of the heterostructure crystal, demonstrating the possibility of fabricating high-resolution pixel arrays of switchable photodiodes (Figure 4f,g) [96].

5. Friction Force Microscopy

Friction Force microscopy (FFM) [99], also known as Lateral Force Microscopy (LFM), can detect lateral force variations on the atomic scale when sliding a sharp tip over a flat surface [100]. The essential feature of the method is that AFM is operated and controlled in the conventional contact mode, but that torsional deformations of the cantilever are monitored. Calculations of quantities such as lateral contact stiffness, friction force, and shear strength are possible after proper calibration procedures [101,102]. LFM was used to identify graphene on rough substrates, and to map the crystallographic orientation of the domains nondestructively, reproducibly, and at high resolution [103]. The atomic-scale friction of an MoS_2 surface was studied by Fujisawa et al. [104], confirming the existence of two-dimensionally discrete friction, due to spatially discrete adhesion and jumps corresponding to the lattice periodicity. The nanoscale frictional characteristics of atomically-thin sheets of different 2D materials exfoliated onto a weakly adherent substrate, such as silicon oxide, were compared to those of their bulk counterparts by Lee et al, showing a monotonically increased friction as the number of layers decreased [105]. Interestingly, the use of a strongly adherent substrate, such as mica, suppressed the trend. Different domains differing by their friction characteristics, and having a periodicity of 180°, were observed on exfoliated monolayer graphene by using angle-dependent scanning, with the friction anisotropy decreasing with an increased applied load (Figure 5a,b) [106]. It was proposed that the domains arise from ripple distortions as a result of anisotropic puckering deformation, due to the tip pushing the ripple crests forward along the scanning direction [105].

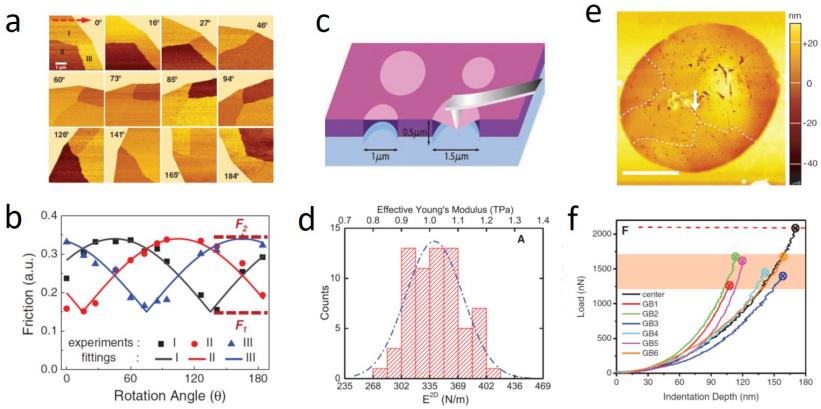

Figure 5. (**a**) Friction force images showing the changing friction contrast of different graphene domains as the sample is rotated from 0° to 184° relative to the horizontal scan direction (red arrow); The plot in (**b**) represents the normalized friction force vs. the rotation angle for three different domains, showing a 180° periodicity (reproduced from [106]); (**c**) Schematic of nanoindentation on a suspended graphene membrane and (**d**) histogram of the elastic modulus measured from force-distance curves on the graphene membrane (adapted from [107]); (**e**) AFM topography of a suspended graphene membrane showing grain boundaries (marked by dashed lines); (**f**) AFM indentation curves showing that fracture occurs at a slightly lower load when AFM tip indents on the grain boundary (reproduced from [108]).

6. Force Spectroscopy

In most AFM applications, the image contrast is obtained from the short range repulsion occurring when the electron orbitals of the tip and the sample overlap, in the so-called Born repulsion regime. However, further interactions can occur and can be used to investigate different properties of the materials when AFM is used in Force Spectroscopy mode. The probe is moved towards the sample in the normal direction and the vertical position and the deflection of the cantilever are recorded and converted to force vs. distance curves, from which several kinds of information on the mechanical properties of the samples, such as elastic modulus and breaking strength, can be obtained [109,110].

The elastic properties of three-dimensional (3D) materials are commonly described by the elastic modulus E. E is also called Young's modulus when the applied strain is uniaxial, with E = σ/ε, where σ is stress and ε is strain. The maximum tension that a material can withstand represents its tensile strength. Elastic modulus and tensile strength have units of J/m^3 or Pa. In 2D, however, these parameters are normalized by the planar elastic energy, leading to units of J/m^2 or N/m. Although 2D modulus and strength are more suitable to describe 2D materials, for the purpose of comparison between 2D and 3D materials, these 2D parameters are normally converted to 3D ones by dividing the 2D values with the thickness of the sample [111].

The elastic properties and intrinsic breaking strengths of monolayer graphene membranes were measured for the first time by AFM by Lee et al. in 2008 (see Figure 5c,d) [107]. For this purpose, graphene flakes were deposited onto a substrate patterned with an array of circular wells. Free-standing monolayer membranes could be obtained to be probed by nanoindentation with the AFM probe. This method has been applied extensively and the principle is described here below.

When the tip radius is $r_{tip} < r_{hole}$, the load force (F) applied by the AFM tip is related to the deformation geometry of the membrane:

$$F = \left(\sigma_0^{2D}\pi\right)\delta + \left(E^{2D}\frac{q^3}{r^2}\right)\delta^3, \quad (2)$$

being δ the indentation depth at the center of the membrane, r the hole radius, q a dimensionless constant determined by the Poisson's ratio ν of the membrane, and E^{2D} and ${\sigma_0}^{2D}$ the 2D modulus and the 2D pretension respectively. The indentation depth is determined by the displacement of the scanning piezo-tube of the AFM (Δz_p) and the deflection of the AFM tip (Δz_t), and the applied load is obtained by multiplying the deflection of the AFM cantilever with its spring constant. E^{2D} and ${\sigma_0}^{2D}$ can be derived by a least-square fitting of the experimental force-displacement curve (F(d)). With the same setup, also the maximum stress for a tightly clamped, linear elastic, and circular membrane under a spherical indenter can be calculated as:

$$\sigma_m^{2D} = \left(\frac{FE^{2D}}{4\pi r_{tip}}\right)^{1/2}, \quad (3)$$

where F is the breaking force, and r_{tip} is the tip radius. Accurate quantitative measurements require the calibration of geometrical and mechanical properties of the tip, as well as the choice of a suitable model for describing the cantilever-tip-sample system [112].

The force-displacement behavior for a monolayer graphene was interpreted within a framework of nonlinear elastic stress-strain response and showed a breaking strength of a defect-free layer of 42 N m^{-1} and a Young's modulus of E = 1.0 TPa (Figure 5d), representing graphene as the strongest material ever measured, and showing that atomically perfect nanoscale materials can be mechanically tested to deformations well beyond the linear regime [107]. The elastic properties of multilayer flakes with thicknesses (h) varying from 2.4 to 33 nm (8 to 100 layers) could also be extracted from force-distance curves [113]. The extracted bending rigidity was found to increase strongly (proportional to h^3) for thicknesses below 10 nm. Thicker flakes were found to have a smaller bending rigidity,

possibly because of the presence of stacking defects in the flakes. The stable sp^2 bonds forming the graphene lattice compete against changes in length and angle, yielding a very high tensile energy when strained; at the same time, bending a graphene layer does not lead to significant deformation of the sp^2 bonds, thus resulting in its impressive Young's modulus [114]. However, these properties can be modified by the presence of defects or chemistry. The dependence of the elastic properties of graphene on the presence of defects was addressed by Zandiatashbar et al., who employed a modified oxygen plasma technique to induce defects in pristine graphene in a controlled manner [115]. By looking at the evolution of Raman spectra as a function of sheet defectiveness, they were able to categorize the defects as being predominantly sp^3-type (partial oxidation), or predominantly vacancy-type. The 2D elastic modulus (E^{2D}) was found to remain constant over the sp^3-type defect regions, indicating that these defects do not appreciably affect the stiffness. In the vacancy-type defect regions, instead, E^{2D} decreased with increasing defect density, reaching about 30% of the stiffness of the pristine sheet at the maximum exposure time. The breaking strength was found to decrease only about 14% with respect to pristine graphene, meaning that in the sp^3-type defect regime, the elastic stiffness of defective graphene is not significantly diminished in comparison with its pristine counterpart. Under longer plasma exposure, a significant number of carbon atoms were expected to be physically removed from the graphene lattice, as the density of defects increases and adjacent defects coalesce to form bigger voids or extended cavities, so that a dramatic drop in elastic stiffness and strength was expected. Interestingly, the elastic modulus of highly defective, plasma treated graphene (0.3 TPa) was found to be comparable to that measured by AFM indentation for graphene oxide (GO) (0.256 ± 0.028 TPa) [116] and by topographical AFM imaging of wrinkled flakes (0.23 ± 0.07 TPa) [117]. The latter approach revealed significant local heterogeneity in the in-plane elastic modulus of such materials, which is also evidenced by a certain variability of the value reported by different groups [118,119]. The discrepancy in the elastic modulus of GO was attributed to defect concentration or clustering of different functional groups. The ring opening of the epoxide functions and the subsequent formation of ether groups in the basal plane of GO was the origin of plasticity and ductility in n-butylamine-modified GO, which showed an elastic modulus 13% lower than that of the original GO [116]. The conductivity of reduced graphene oxide sheets was shown to scale inversely with the elastic modulus. Theoretical predictions confirmed that the sheets with higher elastic modulus and lower conductivity could be assigned to those of higher oxygen content [120].

The strength of graphene was found to be only slightly reduced by the presence of grain boundaries. Nanoindentation tests showed that fracture loads at the grain boundaries are 20 to 40% smaller than in pristine graphene, representing at most a 15% reduction of the intrinsic strength (Figure 5e,f) [108]. Lee et al. used hierarchical patterning to obtain conformal wrinkling with a soft skin layer [121]. The wrinkle wavelength could be finely controlled by tuning the skin layer's thickness. Force curves measured locally on the peaks of the wrinkles suggested an increase of stiffness with the wavelength, from 14.67 nN/nm for λ ~160 nm to 96.97 nN/nm for λ ~450 nm. Adhesion forces between the surface and tip were nearly invariant (~10 nN on valleys and ~18 nN on peaks) for all of the graphene wrinkles, while a much smaller adhesive force (~3 nN) was expectedly measured on crumples since these features are delaminated from the surface.

Similar studies have also been performed on other 2D membranes. MoS_2 monolayers measured by AFM nanoindentation showed a Young's modulus of 300 GPa [122], comparable to that of steel, only one third lower than exfoliated graphene, and higher than other 2D crystals such as reduced graphene oxide (0.2 TPa) [120], hexagonal boron nitride (0.25 TPa) [123], or carbon nanosheets (10–50 GPa) [124]. The average breaking strength of 23 GPa was found to correspond to the theoretical intrinsic strength of the Mo-S bond, indicating that the material can be highly crystalline and almost free of defects and dislocations [125]. The elastic properties of freely suspended MoS_2 sheets with thicknesses ranging from 5 to 25 layers were also investigated [122]. The thinnest sheets (up to 8 layers) presented strongly nonlinear force-displacement traces, while in sheets thicker than 10 layers

the force-displacement traces were linear, indicating a trade-off between a bending-dominated and a stretching-dominated behavior.

It is worth mentioning that SPM nanoindentations do not leave the atomically thin membrane mechanically undisturbed during measurements [126,127]. Local membrane deformations at the location of the scanning tip are produced. When localized strains are induced in suspended few-layer graphene, the strain distribution under and around the AFM tip could be indeed mapped in situ using hyperspectral Raman imaging via the strain-dependent frequency shifts of the few-layer graphene's G and 2D Raman bands [128]. The contact of the nm-sized scanning probe tip resulted in a two-dimensional strain field with μm dimensions in the suspended membrane. Such deformations and the resulting localized strain distribution in the two-dimensional material can complicate SPM measurement interpretation, and also lead to degradation in the two-dimensional material upon measurement. From a different perspective, in most two-dimensional materials, the application of strain could also lead to changes in opto-electronic properties, which allows for the strain engineering of the material's properties. This opens a way to probe such strain-dependent opto-electronic properties based on the application of localized strain through SPM-based techniques.

7. Strain Engineering and Piezoresponse Force Microscopy

The possibility of finely tuning material properties is highly desirable for a wide range of applications, and strain engineering has been introduced as an interesting way to achieve it [28]. In bulk materials, however, the tuning range is limited by plastic behavior and low fracture limit due to the presence of defects and dislocations. Atomically-thin membranes instead exhibit high elasticity and breaking strength, which makes them sound candidates for engineering their properties via strain.

When graphene is deformed, the unit cell area of graphene would be changed by stretching or compressing. The strain-induced shift of carbon atoms would affect the band structure and therefore the electronic properties. The carrier density would be decreased or increased, and the Fermi level and the work function would change accordingly. The work function of graphene, measured by KPFM, was found to increase with increasing uniaxial strain, reaching a variation as large as 161 meV under a 7% strain, which can be explained by the strain-induced change of the density of states [129]. The dependence of the work function on strain is closely related to graphene's topography, and could be weakened by the presence of ripples (Figure 6a,b) [129]. The conductivity of graphene, however, could be preserved even under structural deformation. C-AFM measurements on wrinkled graphene showed that the current at a fixed bias was similar across the boundaries between crumples and wrinkle domains with different wavelengths, despite the presence of such defective structures having shown a clear effect on stiffness and adhesion [121]. The effect of mechanical strain on the electrical conductivity of suspended MoS_2 membranes was probed by positioning the AFM tip in the center of a flake connected to two microfabricated electrodes. The nanosheet was deformed by the AFM tip while measuring the current flowing between the electrodes (Figure 6c,d). The current increased as soon as the membrane began to deform, reaching a value around four times higher at maximum deformation. The effect was reversible, as the current followed the opposite trend and returned to its pre-deformation value as the tip was fully retracted [130]. This observed piezoresistive behavior can be understood in terms of band gap reduction under tensile strain. At different reduction/strain rates, the piezoresistive effect could be also tuned for monolayer, bilayer, and trilayer MoS_2, because of the different orbital contributions of the band-edge states and their different hybridization [130]. MoS_2 is expected to exhibit piezoelectric effects because of the non-centrosymmetric arrangement of the Mo and S atoms, which develop asymmetrical electrical dipoles when the material is subjected to external stress.

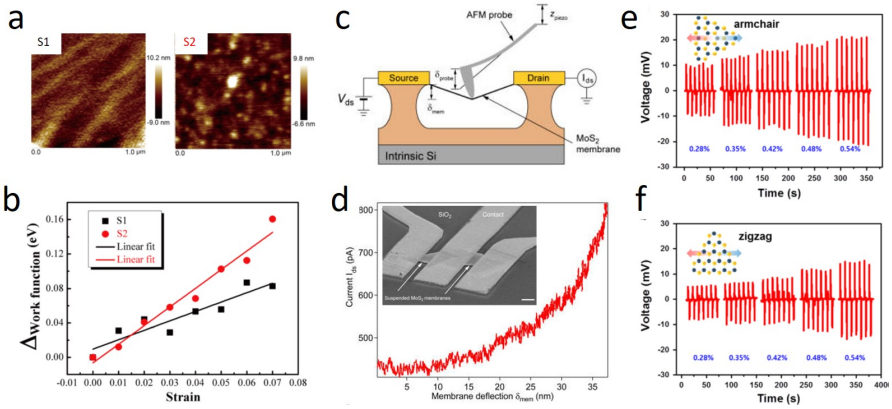

Figure 6. (**a**) AFM images of graphene with (S1) and without (S2) ripples; (**b**) Work function variation of graphene with (S1) and without (S2) ripples as a function of uniaxial strain measured by KPFM. (adapted from [129]); (**c**) Schematic drawing of the setup for direct current electrical characterization of suspended channel MoS_2 devices under strain. The suspended atomically thin membrane (see inset in d) is deformed at the center using an AFM probe; (**d**) Plot of the current vs. membrane deformation measured when a voltage is applied between source and drain electrodes (adapted from [130]). Output voltage obtained from a monolayer MoS_2 as a function of applied strain applied along the armchair direction (**e**) and the zigzag direction (**f**) (reproduced from [131]).

For piezoelectric materials, an applied voltage causes an expansion or a contraction of polarized domains, which in turn results in a measurable deflection of the cantilever. This phenomenon is used in Piezoresponse Force Microscopy (PFM) [132]. In PFM, the tip is brought in contact with the surface and the electromechanical response of the surface is detected as the first-harmonic component of the bias induced tip deflection:

$$d = d_0 + A\cos(\omega t + \varphi), \tag{4}$$

where φ is the phase, which yields information on the polarization direction below the tip. For c- domains, i.e., when the polarization vector is pointing downward, the application of a positive tip bias results in the expansion of the sample, and the surface oscillations are in phase with the tip voltage, $\varphi = 0$. For c+ domains, $\varphi = 180°$. The amplitude A defines the local electromechanical response and depends on the geometry of the tip-surface system and the material's properties [133,134].

Vertical piezoresponse from single-layer graphene was observed by PFM. The calculated vertical piezocoefficient was found to be about 1.4 nm/V, which is much higher than that of conventional piezoelectric materials [135]. Atomically-thin graphene nitride also exhibits anomalous piezoelectricity, due to the fact that a stable phase of a sheet features regularly spaced triangular holes, as indicated by ab initio calculations [136]. Directional dependent piezoelectric effects in chemical vapor deposited MoS_2 monolayers were measured through lateral PFM when an electric field was applied laterally across the flakes [131]. The piezoelectric coefficient was found to be 3.78 pm/V in the armchair direction, and 1.38 pm/V in the zigzag direction, clearly revealing its distinct anisotropic piezoresponse in single-crystalline monolayers (Figure 6d,e).

8. Conclusions

Two-dimensional (2D) nanosheets are an emerging new class of materials, and new ways to define and quantify their structure-function relationships are required. Features such as average flake size, shape, concentration, and density of defects present at the chemical level are among the most significant properties affecting these materials' function. The wealth of scientific reports described in this review and beyond confirms the usefulness of Scanning Probe Microscopy as an efficient and valuable multilevel tool for atomic- and nanoscale 2D materials characterization, from structural and morphological, to (opto-)electronic and mechanical perspectives.

Because mechanical properties play vital roles in the design of flexible, stretchable, and epidermal electronics that may potentially dominate the future electronics industry [111], particular attention has been dedicated to this aspect here. The mechanics of 2D atomically-thin materials, their behavior under stress and electrical fields, and the interactions between adjacent sheets, between sheets and a substrate, or between sheets and their environment should be better understood to optimize the level of performance that shall be achieved. Thus, new concepts are required for modeling these materials. The coupling between piezoelectric polarization and semiconductor properties, such as electronic transport and photoresponse, is expected to give rise to unprecedented device characteristics [137,138]. The emerging fields of piezotronics and piezo-phototronics, which propose new means of manipulating charge-carrier transport in the operation of flexible devices through the application of external mechanical stimuli [139], demonstrate the need for the correlative characterization of mechanical and electronic properties at the single layer level, therefore opening new opportunities for the unceasing development of SPMs.

Conflicts of Interest: The author declares no conflict of interest.

References

1. Schwierz, F. Graphene transistors. *Nat. Nanotechnol.* **2010**, *5*, 487–496. [CrossRef] [PubMed]
2. Jariwala, D.; Sangwan, V.K.; Lauhon, L.J.; Marks, T.J.; Hersam, M.C. Emerging device applications for semiconducting two-dimensional transition metal dichalcogenides. *ACS Nano* **2014**, *8*, 1102–1120. [CrossRef] [PubMed]
3. Cain, J.D.; Hanson, E.D.; Shi, F.; Dravid, V.P. Emerging opportunities in the two-dimensional chalcogenide systems and architecture. *Curr. Opin. Solid State Mater. Sci.* **2016**, *20*, 374–387. [CrossRef]
4. Allen, M.J.; Tung, V.C.; Kaner, R.B. Honeycomb carbon: A review of graphene. *Chem. Rev.* **2010**, *110*, 132–145. [CrossRef] [PubMed]
5. Novoselov, K.S.; Geim, A.K.; Morozov, S.V.; Jiang, D.; Katsnelson, M.I.; Grigorieva, I.V.; Dubonos, S.V.; Firsov, A.A. Two-dimensional gas of massless dirac fermions in graphene. *Nature* **2005**, *438*, 197–200. [CrossRef] [PubMed]
6. Zhang, Y.; Tan, Y.-W.; Stormer, H.L.; Kim, P. Experimental observation of the quantum hall effect and berry's phase in graphene. *Nature* **2005**, *438*, 201–204. [CrossRef] [PubMed]
7. Geim, A.K.; Novoselov, K.S. The rise of graphene. *Nat. Mater.* **2007**, *6*, 183–191. [CrossRef] [PubMed]
8. Castro Neto, A.H.; Guinea, F.; Peres, N.M.R.; Novoselov, K.S.; Geim, A.K. The electronic properties of graphene. *Rev. Mod. Phys.* **2009**, *81*, 109–162. [CrossRef]
9. Geim, A.K. Graphene: Status and prospects. *Science* **2009**, *324*, 1530–1534. [CrossRef] [PubMed]
10. Butler, S.Z.; Hollen, S.M.; Cao, L.; Cui, Y.; Gupta, J.A.; Gutiérrez, H.R.; Heinz, T.F.; Hong, S.S.; Huang, J.; Ismach, A.F.; et al. Progress, challenges, and opportunities in two-dimensional materials beyond graphene. *ACS Nano* **2013**, *7*, 2898–2926. [CrossRef] [PubMed]
11. Geim, A.K.; Grigorieva, I.V. Van der Waals heterostructures. *Nature* **2013**, *499*, 419–425. [CrossRef] [PubMed]
12. Wang, F.; Wang, Z.; Xu, K.; Wang, F.; Wang, Q.; Huang, Y.; Yin, L.; He, J. Tunable gate-MoS_2 Van der Waals p–n junctions with novel optoelectronic performance. *Nano Lett.* **2015**, *15*, 7558–7566. [CrossRef] [PubMed]
13. Radisavljevic, B.; Radenovic, A.; Brivio, J.; Giacometti, V.; Kis, A. Single-layer MoS_2 transistors. *Nat. Nanotechnol.* **2011**, *6*, 147–150. [CrossRef] [PubMed]
14. Wang, H.; Yu, L.; Lee, Y.-H.; Shi, Y.; Hsu, A.; Chin, M.L.; Li, L.-J.; Dubey, M.; Kong, J.; Palacios, T. Integrated circuits based on bilayer MoS_2 transistors. *Nano Lett.* **2012**, *12*, 4674–4680. [CrossRef] [PubMed]
15. Krasnozhon, D.; Lembke, D.; Nyffeler, C.; Leblebici, Y.; Kis, A. MoS_2 transistors operating at gigahertz frequencies. *Nano Lett.* **2014**, *14*, 5905–5911. [CrossRef] [PubMed]
16. Lee, S.; Sohn, J.; Jiang, Z.; Chen, H.-Y.; Philip Wong, H.S. Metal oxide-resistive memory using graphene-edge electrodes. *Nat. Commun.* **2015**, *6*, 8407. [CrossRef] [PubMed]
17. Han, S.-T.; Zhou, Y.; Chen, B.; Wang, C.; Zhou, L.; Yan, Y.; Zhuang, J.; Sun, Q.; Zhang, H.; Roy, V.A.L. Hybrid flexible resistive random access memory-gated transistor for novel nonvolatile data storage. *Small* **2016**, *12*, 390–396. [CrossRef] [PubMed]

18. Sangwan, V.K.; Jariwala, D.; Kim, I.S.; Chen, K.-S.; Marks, T.J.; Lauhon, L.J.; Hersam, M.C. Gate-tunable memristive phenomena mediated by grain boundaries in single-layer MoS_2. *Nat. Nano* **2015**, *10*, 403–406. [CrossRef] [PubMed]
19. Musumeci, C.; Liscio, A.; Palermo, V.; Samorì, P. Electronic characterization of supramolecular materials at the nanoscale by conductive atomic force and kelvin probe force microscopies. *Mater. Today* **2014**, *17*, 504. [CrossRef]
20. Liscio, A.; Palermo, V.; Samorì, P. Nanoscale quantitative measurement of the potential of charged nanostructures by electrostatic and kelvin probe force microscopy: Unraveling electronic processes in complex materials. *Acc. Chem. Res.* **2010**, *43*, 541–550. [CrossRef] [PubMed]
21. Deshpande, A.; LeRoy, B.J. Scanning probe microscopy of graphene. *Phys. E* **2012**, *44*, 743–759. [CrossRef]
22. Meyer, J.C.; Geim, A.K.; Katsnelson, M.I.; Novoselov, K.S.; Booth, T.J.; Roth, S. The structure of suspended graphene sheets. *Nature* **2007**, *446*, 60–63. [CrossRef] [PubMed]
23. Fasolino, A.; Los, J.H.; Katsnelson, M.I. Intrinsic ripples in graphene. *Nat. Mater.* **2007**, *6*, 858–861. [CrossRef] [PubMed]
24. Miao, F.; Wijeratne, S.; Zhang, Y.; Coskun, U.C.; Bao, W.; Lau, C.N. Phase-coherent transport in graphene quantum billiards. *Science* **2007**, *317*, 1530–1533. [CrossRef] [PubMed]
25. Yazyev, O.V.; Chen, Y.P. Polycrystalline graphene and other two-dimensional materials. *Nat. Nano* **2014**, *9*, 755–767. [CrossRef] [PubMed]
26. Zhang, Z.; Zou, X.; Crespi, V.H.; Yakobson, B.I. Intrinsic magnetism of grain boundaries in two-dimensional metal dichalcogenides. *ACS Nano* **2013**, *7*, 10475–10481. [CrossRef] [PubMed]
27. Zou, X.; Yakobson, B.I. An open canvas—2D materials with defects, disorder, and functionality. *Acc. Chem. Res.* **2015**, *48*, 73–80. [CrossRef] [PubMed]
28. Rafael, R.; Andrés, C.-G.; Emmanuele, C.; Francisco, G. Strain engineering in semiconducting two-dimensional crystals. *J. Phys. Condens. Matter* **2015**, *27*, 313201.
29. Binnig, G.; Rohrer, H.; Gerber, C.; Weibel, E. Surface studies by scanning tunneling microscopy. *Phys. Rev. Lett.* **1982**, *49*, 57–61. [CrossRef]
30. Zhang, R.; Ivey, D.G. Preparation of sharp polycrystalline tungsten tips for scanning tunneling microscopy imaging. *J. Vac. Sci. Technol. B* **1996**, *14*, 1–10. [CrossRef]
31. Khan, Y.; Al-Falih, H.; Zhang, Y.; Ng, T.K.; Ooi, B.S. Two-step controllable electrochemical etching of tungsten scanning probe microscopy tips. *Rev. Sci. Instrum.* **2012**, *83*, 063708. [CrossRef] [PubMed]
32. Yamada, T.K.; Abe, T.; Nazriq, N.M.K.; Irisawa, T. Electron-bombarded <110>-oriented tungsten tips for stable tunneling electron emission. *Rev. Sci. Instrum.* **2016**, *87*, 033703. [CrossRef] [PubMed]
33. Stolyarova, E.; Rim, K.T.; Ryu, S.; Maultzsch, J.; Kim, P.; Brus, L.E.; Heinz, T.F.; Hybertsen, M.S.; Flynn, G.W. High-resolution scanning tunneling microscopy imaging of mesoscopic graphene sheets on an insulating surface. *Proc. Natl. Acad. Sci. USA* **2007**, *104*, 9209–9212. [CrossRef] [PubMed]
34. Zhang, Y.; Brar, V.W.; Wang, F.; Girit, C.; Yayon, Y.; Panlasigui, M.; Zettl, A.; Crommie, M.F. Giant phonon-induced conductance in scanning tunnelling spectroscopy of gate-tunable graphene. *Nat. Phys.* **2008**, *4*, 627–630. [CrossRef]
35. Ishigami, M.; Chen, J.H.; Cullen, W.G.; Fuhrer, M.S.; Williams, E.D. Atomic structure of graphene on SiO_2. *Nano Lett.* **2007**, *7*, 1643–1648. [CrossRef] [PubMed]
36. Berger, C.; Song, Z.; Li, X.; Wu, X.; Brown, N.; Naud, C.; Mayou, D.; Li, T.; Hass, J.; Marchenkov, A.N.; et al. Electronic confinement and coherence in patterned epitaxial graphene. *Science* **2006**, *312*, 1191–1196. [CrossRef] [PubMed]
37. Moran-Meza, J.A.; Cousty, J.; Lubin, C.; Thoyer, F. Understanding the STM images of epitaxial graphene on a reconstructed 6H-SiC(0001) surface: The role of tip-induced mechanical distortion of graphene. *Phys. Chem. Chem. Phys.* **2016**, *18*, 14264–14272. [CrossRef] [PubMed]
38. Coraux, J.; N'Diaye, A.T.; Busse, C.; Michely, T. Structural coherency of graphene on Ir(111). *Nano Lett.* **2008**, *8*, 565–570. [CrossRef] [PubMed]
39. Kwon, S.-Y.; Ciobanu, C.V.; Petrova, V.; Shenoy, V.B.; Bareño, J.; Gambin, V.; Petrov, I.; Kodambaka, S. Growth of semiconducting graphene on palladium. *Nano Lett.* **2009**, *9*, 3985–3990. [CrossRef] [PubMed]
40. Gao, L.; Guest, J.R.; Guisinger, N.P. Epitaxial graphene on Cu(111). *Nano Lett.* **2010**, *10*, 3512–3516. [CrossRef] [PubMed]

41. Dubout, Q.; Calleja, F.; Sclauzero, G.; Etzkorn, M.; Lehnert, A.; Claude, L.; Papagno, M.; Natterer, F.D.; Patthey, F.; Rusponi, S.; et al. Giant apparent lattice distortions in STM images of corrugated sp^2-hybridised monolayers. *New J. Phys.* **2016**, *18*, 103027. [CrossRef]
42. Xue, J.; Sanchez-Yamagishi, J.; Bulmash, D.; Jacquod, P.; Deshpande, A.; Watanabe, K.; Taniguchi, T.; Jarillo-Herrero, P.; LeRoy, B.J. Scanning tunnelling microscopy and spectroscopy of ultra-flat graphene on hexagonal boron nitride. *Nat. Mater.* **2011**, *10*, 282–285. [CrossRef] [PubMed]
43. Harners, R.J. Atomic-resolution surface spectroscopy with the scanning tunneling microscope. *Annu. Rev. Phys. Chem.* **1989**, *40*, 531–559.
44. Tromp, R.M. Spectroscopy with the scanning tunnelling microscope: A critical review. *J. Phys. Condens. Matter* **1989**, *1*, 10211. [CrossRef]
45. Liu, H.; Zheng, H.; Yang, F.; Jiao, L.; Chen, J.; Ho, W.; Gao, C.; Jia, J.; Xie, M. Line and point defects in $MoSe_2$ bilayer studied by scanning tunneling microscopy and spectroscopy. *ACS Nano* **2015**, *9*, 6619–6625. [CrossRef] [PubMed]
46. Park, J.H.; Vishwanath, S.; Liu, X.; Zhou, H.; Eichfeld, S.M.; Fullerton-Shirey, S.K.; Robinson, J.A.; Feenstra, R.M.; Furdyna, J.; Jena, D.; et al. Scanning tunneling microscopy and spectroscopy of air exposure effects on molecular beam epitaxy grown WSe_2 monolayers and bilayers. *ACS Nano* **2016**, *10*, 4258–4267. [CrossRef] [PubMed]
47. Huang, Y.L.; Chen, Y.; Zhang, W.; Quek, S.Y.; Chen, C.-H.; Li, L.-J.; Hsu, W.-T.; Chang, W.-H.; Zheng, Y.J.; Chen, W.; et al. Bandgap tunability at single-layer molybdenum disulphide grain boundaries. *Nat. Commun.* **2015**, *6*, 6298. [CrossRef] [PubMed]
48. Georgi, A.; Nemes-Incze, P.; Carrillo-Bastos, R.; Faria, D.; Viola Kusminskiy, S.; Zhai, D.; Schneider, M.; Subramaniam, D.; Mashoff, T.; Freitag, N.M.; et al. Tuning the pseudospin polarization of graphene by a pseudomagnetic field. *Nano Lett.* **2017**, *17*, 2240–2245. [CrossRef] [PubMed]
49. Philippe, D.; Viet Hung, N.; Jérôme, S.-M. Thermoelectric effects in graphene nanostructures. *J. Phys. Condens. Matter* **2015**, *27*, 133204.
50. Park, J.; He, G.; Feenstra, R.M.; Li, A.-P. Atomic-scale mapping of thermoelectric power on graphene: Role of defects and boundaries. *Nano Lett.* **2013**, *13*, 3269–3273. [CrossRef] [PubMed]
51. Nemes-Incze, P.; Osváth, Z.; Kamarás, K.; Biró, L.P. Anomalies in thickness measurements of graphene and few layer graphite crystals by tapping mode atomic force microscopy. *Carbon* **2008**, *46*, 1435–1442. [CrossRef]
52. Binnig, G.; Quate, C.F.; Gerber, C. Atomic force microscope. *Phys. Rev. Lett.* **1986**, *56*, 930–933. [CrossRef] [PubMed]
53. Wang, Y.; Yang, R.; Shi, Z.; Zhang, L.; Shi, D.; Wang, E.; Zhang, G. Super-elastic graphene ripples for flexible strain sensors. *ACS Nano* **2011**, *5*, 3645–3650. [CrossRef] [PubMed]
54. Burnett, T.L.; Yakimova, R.; Kazakova, O. Identification of epitaxial graphene domains and adsorbed species in ambient conditions using quantified topography measurements. *J. Appl. Phys.* **2012**, *112*, 054308. [CrossRef]
55. Kim, J.-S.; Choi, J.S.; Lee, M.J.; Park, B.H.; Bukhvalov, D.; Son, Y.-W.; Yoon, D.; Cheong, H.; Yun, J.-N.; Jung, Y.; et al. Between Scylla and Charybdis: Hydrophobic graphene-guided water diffusion on hydrophilic substrates. *Sci. Rep.* **2013**, *3*, 2309. [CrossRef] [PubMed]
56. Novoselov, K.S.; Jiang, D.; Schedin, F.; Booth, T.J.; Khotkevich, V.V.; Morozov, S.V.; Geim, A.K. Two-dimensional atomic crystals. *Proc. Natl. Acad. Sci. USA* **2005**, *102*, 10451–10453. [CrossRef] [PubMed]
57. Russo, P.; Compagnini, G.; Musumeci, C.; Pignataro, B. Raman monitoring of strain induced effects in mechanically deposited single layer graphene. *J. Nanosci. Nanotechnol.* **2012**, *12*, 8755–8758. [CrossRef] [PubMed]
58. Robinson, B.J.; Giusca, C.E.; Gonzalez, Y.T.; Kay, N.D.; Kazakova, O.; Kolosov, O.V. Structural, optical and electrostatic properties of single and few-layers MoS_2: Effect of substrate. *2D Mater.* **2015**, *2*, 015005. [CrossRef]
59. Lee, Y.-H.; Zhang, X.-Q.; Zhang, W.; Chang, M.-T.; Lin, C.-T.; Chang, K.-D.; Yu, Y.-C.; Wang, J.T.-W.; Chang, C.-S.; Li, L.-J.; et al. Synthesis of large-area MoS_2 atomic layers with chemical vapor deposition. *Adv. Mater.* **2012**, *24*, 2320–2325. [CrossRef] [PubMed]
60. Mechler, Á.; Kopniczky, J.; Kokavecz, J.; Hoel, A.; Granqvist, C.-G.; Heszler, P. Anomalies in nanostructure size measurements by AFM. *Phys. Rev. B* **2005**, *72*, 125407. [CrossRef]

61. García, R.; San Paulo, A. Attractive and repulsive tip-sample interaction regimes in tapping-mode atomic force microscopy. *Phys. Rev. B* **1999**, *60*, 4961–4967. [CrossRef]
62. Cameron, J.S.; Ashley, D.S.; Andrew, J.S.; Joseph, G.S.; Christopher, T.G. Accurate thickness measurement of graphene. *Nanotechnology* **2016**, *27*, 125704.
63. Ly, T.H.; Chiu, M.-H.; Li, M.-Y.; Zhao, J.; Perello, D.J.; Cichocka, M.O.; Oh, H.M.; Chae, S.H.; Jeong, H.Y.; Yao, F.; et al. Observing grain boundaries in CVD-grown monolayer transition metal dichalcogenides. *ACS Nano* **2014**, *8*, 11401–11408. [CrossRef] [PubMed]
64. Duong, D.L.; Han, G.H.; Lee, S.M.; Gunes, F.; Kim, E.S.; Kim, S.T.; Kim, H.; Ta, Q.H.; So, K.P.; Yoon, S.J.; et al. Probing graphene grain boundaries with optical microscopy. *Nature* **2012**, *490*, 235–239. [CrossRef] [PubMed]
65. Leng, Y.; Williams, C.C. *Molecular Charge Mapping with Electrostatic Force Microscope*; SPIE: Bellingham, WA, USA, 1993; pp. 35–39.
66. Nonnenmacher, M.; O'Boyle, M.P.; Wickramasinghe, H.K. Kelvin probe force microscopy. *Appl. Phys. Lett.* **1991**, *58*, 2921–2923. [CrossRef]
67. O'Shea, S.J.; Atta, R.M.; Murrell, M.P.; Welland, M.E. Conducting atomic force microscopy study of silicon dioxide breakdown. *J. Vac. Sci. Technol. B* **1995**, *13*, 1945–1952. [CrossRef]
68. Avila, A.; Bhushan, B. Electrical measurement techniques in atomic force microscopy. *Crit. Rev. Solid State Mater. Sci.* **2010**, *35*, 38–51. [CrossRef]
69. Coffey, D.C.; Reid, O.G.; Rodovsky, D.B.; Bartholomew, G.P.; Ginger, D.S. Mapping local photocurrents in polymer/fullerene solar cells with photoconductive atomic force microscopy. *Nano Lett.* **2007**, *7*, 738–744. [CrossRef] [PubMed]
70. Jacobs, H.O.; Leuchtmann, P.; Homan, O.J.; Stemmer, A. Resolution and contrast in kelvin probe force microscopy. *J. Appl. Phys.* **1998**, *84*, 1168–1173. [CrossRef]
71. Hormeno, S.; Penedo, M.; Manzano, C.V.; Luna, M. Gold nanoparticle coated silicon tips for kelvin probe force microscopy in air. *Nanotechnology* **2013**, *24*, 395701. [CrossRef] [PubMed]
72. Lanza, M.; Bayerl, A.; Gao, T.; Porti, M.; Nafria, M.; Jing, G.Y.; Zhang, Y.F.; Liu, Z.F.; Duan, H.L. Graphene-coated atomic force microscope tips for reliable nanoscale electrical characterization. *Adv. Mater.* **2013**, *25*, 1440–1444. [CrossRef] [PubMed]
73. Hui, F.; Vajha, P.; Shi, Y.; Ji, Y.; Duan, H.; Padovani, A.; Larcher, L.; Li, X.R.; Xu, J.J.; Lanza, M. Moving graphene devices from lab to market: Advanced graphene-coated nanoprobes. *Nanoscale* **2016**, *8*, 8466–8473. [CrossRef] [PubMed]
74. Kazakova, O.; Panchal, V.; Burnett, T. Epitaxial graphene and graphene-based devices studied by electrical scanning probe microscopy. *Crystals* **2013**, *3*, 191. [CrossRef]
75. Burnett, T.; Yakimova, R.; Kazakova, O. Mapping of local electrical properties in epitaxial graphene using electrostatic force microscopy. *Nano Lett.* **2011**, *11*, 2324–2328. [CrossRef] [PubMed]
76. Panchal, V.; Pearce, R.; Yakimova, R.; Tzalenchuk, A.; Kazakova, O. Standardization of surface potential measurements of graphene domains. *Sci. Rep.* **2013**, *3*, 2597. [CrossRef] [PubMed]
77. Ziegler, D.; Gava, P.; Güttinger, J.; Molitor, F.; Wirtz, L.; Lazzeri, M.; Saitta, A.M.; Stemmer, A.; Mauri, F.; Stampfer, C. Variations in the work function of doped single- and few-layer graphene assessed by kelvin probe force microscopy and density functional theory. *Phys. Rev. B* **2011**, *83*, 235434. [CrossRef]
78. Eriksson, J.; Pearce, R.; Iakimov, T.; Virojanadara, C.; Gogova, D.; Andersson, M.; Syväjärvi, M.; Lloyd Spetz, A.; Yakimova, R. The influence of substrate morphology on thickness uniformity and unintentional doping of epitaxial graphene on SiC. *Appl. Phys. Lett.* **2012**, *100*, 241607. [CrossRef]
79. Long, F.; Yasaei, P.; Sanoj, R.; Yao, W.; Král, P.; Salehi-Khojin, A.; Shahbazian-Yassar, R. Characteristic work function variations of graphene line defects. *ACS Appl. Mater. Interfaces* **2016**, *8*, 18360–18366. [CrossRef] [PubMed]
80. Pearce, R.; Eriksson, J.; Iakimov, T.; Hultman, L.; Lloyd Spetz, A.; Yakimova, R. On the differing sensitivity to chemical gating of single and double layer epitaxial graphene explored using scanning kelvin probe microscopy. *ACS Nano* **2013**, *7*, 4647–4656. [CrossRef] [PubMed]
81. Kulkarni, D.D.; Kim, S.; Chyasnavichyus, M.; Hu, K.; Fedorov, A.G.; Tsukruk, V.V. Chemical reduction of individual graphene oxide sheets as revealed by electrostatic force microscopy. *J. Am. Chem. Soc.* **2014**, *136*, 6546–6549. [CrossRef] [PubMed]
82. Yu, Y.-J.; Zhao, Y.; Ryu, S.; Brus, L.E.; Kim, K.S.; Kim, P. Tuning the graphene work function by electric field effect. *Nano Lett.* **2009**, *9*, 3430–3434. [CrossRef] [PubMed]

83. Fisichella, G.; Greco, G.; Roccaforte, F.; Giannazzo, F. Current transport in graphene/AlGaN/GaN vertical heterostructures probed at nanoscale. *Nanoscale* **2014**, *6*, 8671–8680. [CrossRef] [PubMed]
84. Fisichella, G.; Di Franco, S.; Fiorenza, P.; Lo Nigro, R.; Roccaforte, F.; Tudisco, C.; Condorelli, G.G.; Piluso, N.; Spartà, N.; Lo Verso, S.; et al. Micro- and nanoscale electrical characterization of large-area graphene transferred to functional substrates. *Beilstein J. Nanotechnol.* **2013**, *4*, 234–242. [CrossRef] [PubMed]
85. Kellar, J.A.; Alaboson, J.M.P.; Wang, Q.H.; Hersam, M.C. Identifying and characterizing epitaxial graphene domains on partially graphitized SiC(0001) surfaces using scanning probe microscopy. *Appl. Phys. Lett.* **2010**, *96*, 143103. [CrossRef]
86. Giannazzo, F.; Deretzis, I.; La Magna, A.; Roccaforte, F.; Yakimova, R. Electronic transport at monolayer-bilayer junctions in epitaxial graphene on SiC. *Phys. Rev. B* **2012**, *86*, 235422. [CrossRef]
87. Sonde, S.; Giannazzo, F.; Raineri, V.; Yakimova, R.; Huntzinger, J.R.; Tiberj, A.; Camassel, J. Electrical properties of the graphene/4H-SiC(0001) interface probed by scanning current spectroscopy. *Phys. Rev. B* **2009**, *80*. [CrossRef]
88. Giannazzo, F.; Fisichella, G.; Piazza, A.; Agnello, S.; Roccaforte, F. Nanoscale inhomogeneity of the Schottky barrier and resistivity in MoS_2 multilayers. *Phys. Rev. B* **2015**, *92*. [CrossRef]
89. Bampoulis, P.; van Bremen, R.; Yao, Q.; Poelsema, B.; Zandvliet, H.J.W.; Sotthewes, K. Defect dominated charge transport and fermi level pinning in MoS_2/metal contacts. *ACS Appl. Mater. Interfaces* **2017**, *9*, 19278–19286. [CrossRef] [PubMed]
90. Giannazzo, F.; Fisichella, G.; Greco, G.; Di Franco, S.; Deretzis, I.; La Magna, A.; Bongiorno, C.; Nicotra, G.; Spinella, C.; Scopelliti, M.; et al. Ambipolar MoS_2 transistors by nanoscale tailoring of Schottky barrier using oxygen plasma functionalization. *ACS Appl. Mater. Interfaces* **2017**. [CrossRef] [PubMed]
91. Liu, H.; Hoeppener, S.; Schubert, U.S. Nanoscale materials patterning by local electrochemical lithography. *Adv. Eng. Mater.* **2016**, *18*, 890–902.
92. Mativetsky, J.M.; Treossi, E.; Orgiu, E.; Melucci, M.; Veronese, G.P.; Samorì, P.; Palermo, V. Local current mapping and patterning of reduced graphene oxide. *J. Am. Chem. Soc.* **2010**, *132*, 14130–14136. [CrossRef] [PubMed]
93. Faucett, A.C.; Mativetsky, J.M. Nanoscale reduction of graphene oxide under ambient conditions. *Carbon* **2015**, *95*, 1069–1075. [CrossRef]
94. Byun, I.-S.; Yoon, D.; Choi, J.S.; Hwang, I.; Lee, D.H.; Lee, M.J.; Kawai, T.; Son, Y.-W.; Jia, Q.; Cheong, H.; et al. Nanoscale lithography on monolayer graphene using hydrogenation and oxidation. *ACS Nano* **2011**, *5*, 6417–6424. [CrossRef] [PubMed]
95. Mativetsky, J.M.; Liscio, A.; Treossi, E.; Orgiu, E.; Zanelli, A.; Samorì, P.; Palermo, V. Graphene transistors via in situ voltage-induced reduction of graphene-oxide under ambient conditions. *J. Am. Chem. Soc.* **2011**, *133*, 14320–14326. [CrossRef] [PubMed]
96. Son, Y.; Li, M.-Y.; Cheng, C.-C.; Wei, K.-H.; Liu, P.; Wang, Q.H.; Li, L.-J.; Strano, M.S. Observation of switchable photoresponse of a monolayer WSe_2–MoS_2 lateral heterostructure via photocurrent spectral atomic force microscopic imaging. *Nano Lett.* **2016**, *16*, 3571–3577. [CrossRef] [PubMed]
97. Ruzmetov, D.; Zhang, K.; Stan, G.; Kalanyan, B.; Bhimanapati, G.R.; Eichfeld, S.M.; Burke, R.A.; Shah, P.B.; O'Regan, T.P.; Crowne, F.J.; et al. Vertical 2D/3D semiconductor heterostructures based on epitaxial molybdenum disulfide and gallium nitride. *ACS Nano* **2016**, *10*, 3580–3588. [CrossRef] [PubMed]
98. Son, Y.; Wang, Q.H.; Paulson, J.A.; Shih, C.-J.; Rajan, A.G.; Tvrdy, K.; Kim, S.; Alfeeli, B.; Braatz, R.D.; Strano, M.S. Layer number dependence of MoS_2 photoconductivity using photocurrent spectral atomic force microscopic imaging. *ACS Nano* **2015**, *9*, 2843–2855. [CrossRef] [PubMed]
99. Mate, C.M.; McClelland, G.M.; Erlandsson, R.; Chiang, S. Atomic-scale friction of a tungsten tip on a graphite surface. *Phys. Rev. Lett.* **1987**, *59*, 1942–1945. [CrossRef] [PubMed]
100. Bennewitz, R. Friction force microscopy. *Mater. Today* **2005**, *8*, 42–48. [CrossRef]
101. Cain, R.G.; Biggs, S.; Page, N.W. Force calibration in lateral force microscopy. *J. Colloid Interface Sci.* **2000**, *227*, 55–65. [CrossRef] [PubMed]
102. Gibson, C.T.; Watson, G.S.; Myhra, S. Lateral force microscopy—A quantitative approach. *Wear* **1997**, *213*, 72–79. [CrossRef]
103. Marsden, A.J.; Phillips, M.; Wilson, N.R. Friction force microscopy: A simple technique for identifying graphene on rough substrates and mapping the orientation of graphene grains on copper. *Nanotechnology* **2013**, *24*, 255704. [CrossRef] [PubMed]

104. Fujisawa, S.; Kishi, E.; Sugawara, Y.; Morita, S. Atomic-scale friction observed with a two-dimensional frictional-force microscope. *Phys. Rev. B* **1995**, *51*, 7849–7857. [CrossRef]
105. Lee, C.; Li, Q.; Kalb, W.; Liu, X.-Z.; Berger, H.; Carpick, R.W.; Hone, J. Frictional characteristics of atomically thin sheets. *Science* **2010**, *328*, 76–80. [CrossRef] [PubMed]
106. Choi, J.S.; Kim, J.-S.; Byun, I.-S.; Lee, D.H.; Lee, M.J.; Park, B.H.; Lee, C.; Yoon, D.; Cheong, H.; Lee, K.H.; et al. Friction anisotropy–driven domain imaging on exfoliated monolayer graphene. *Science* **2011**, *333*, 607–610. [CrossRef] [PubMed]
107. Lee, C.; Wei, X.; Kysar, J.W.; Hone, J. Measurement of the elastic properties and intrinsic strength of monolayer graphene. *Science* **2008**, *321*, 385–388. [CrossRef] [PubMed]
108. Lee, G.-H.; Cooper, R.C.; An, S.J.; Lee, S.; van der Zande, A.; Petrone, N.; Hammerberg, A.G.; Lee, C.; Crawford, B.; Oliver, W.; et al. High-strength chemical-vapor–deposited graphene and grain boundaries. *Science* **2013**, *340*, 1073–1076. [CrossRef] [PubMed]
109. Butt, H.-J.; Cappella, B.; Kappl, M. Force measurements with the atomic force microscope: Technique, interpretation and applications. *Surf. Sci. Rep.* **2005**, *59*, 1–152. [CrossRef]
110. Cappella, B.; Dietler, G. Force-distance curves by atomic force microscopy. *Surf. Sci. Rep.* **1999**, *34*, 1–104. [CrossRef]
111. Liu, K.; Wu, J. Mechanical properties of two-dimensional materials and heterostructures. *J. Mater. Res.* **2016**, *31*, 832–844. [CrossRef]
112. Hutter, J.L.; Bechhoefer, J. Calibration of atomic-force microscope tips. *Rev. Sci. Instrum.* **1993**, *64*, 1868–1873. [CrossRef]
113. Poot, M.; van der Zant, H.S.J. Nanomechanical properties of few-layer graphene membranes. *Appl. Phys. Lett.* **2008**, *92*, 063111. [CrossRef]
114. Palermo, V.; Kinloch, I.A.; Ligi, S.; Pugno, N.M. Nanoscale mechanics of graphene and graphene oxide in composites: A scientific and technological perspective. *Adv. Mater.* **2016**, *28*, 6232–6238. [CrossRef] [PubMed]
115. Zandiatashbar, A.; Lee, G.-H.; An, S.J.; Lee, S.; Mathew, N.; Terrones, M.; Hayashi, T.; Picu, C.R.; Hone, J.; Koratkar, N. Effect of defects on the intrinsic strength and stiffness of graphene. *Nat. Commun.* **2014**, *5*, 3186. [CrossRef] [PubMed]
116. Wei, X.; Mao, L.; Soler-Crespo, R.A.; Paci, J.T.; Huang, J.; Nguyen, S.T.; Espinosa, H.D. Plasticity and ductility in graphene oxide through a mechanochemically induced damage tolerance mechanism. *Nat. Commun.* **2015**, *6*, 8029. [CrossRef] [PubMed]
117. Kunz, D.A.; Feicht, P.; Gödrich, S.; Thurn, H.; Papastavrou, G.; Fery, A.; Breu, J. Space-resolved in-plane moduli of graphene oxide and chemically derived graphene applying a simple wrinkling procedure. *Adv. Mater.* **2013**, *25*, 1337–1341. [CrossRef] [PubMed]
118. Cao, C.; Daly, M.; Singh, C.V.; Sun, Y.; Filleter, T. High strength measurement of monolayer graphene oxide. *Carbon* **2015**, *81*, 497–504. [CrossRef]
119. Suk, J.W.; Piner, R.D.; An, J.; Ruoff, R.S. Mechanical properties of monolayer graphene oxide. *ACS Nano* **2010**, *4*, 6557–6564. [CrossRef] [PubMed]
120. Gómez-Navarro, C.; Burghard, M.; Kern, K. Elastic properties of chemically derived single graphene sheets. *Nano Lett.* **2008**, *8*, 2045–2049. [CrossRef] [PubMed]
121. Lee, W.-K.; Kang, J.; Chen, K.-S.; Engel, C.J.; Jung, W.-B.; Rhee, D.; Hersam, M.C.; Odom, T.W. Multiscale, hierarchical patterning of graphene by conformal wrinkling. *Nano Lett.* **2016**, *16*, 7121–7127. [CrossRef] [PubMed]
122. Castellanos-Gomez, A.; Poot, M.; Steele, G.A.; van der Zant, H.S.J.; Agraït, N.; Rubio-Bollinger, G. Elastic properties of freely suspended MoS_2 nanosheets. *Adv. Mater.* **2012**, *24*, 772–775. [CrossRef] [PubMed]
123. Song, L.; Ci, L.; Lu, H.; Sorokin, P.B.; Jin, C.; Ni, J.; Kvashnin, A.G.; Kvashnin, D.G.; Lou, J.; Yakobson, B.I.; et al. Large scale growth and characterization of atomic hexagonal boron nitride layers. *Nano Lett.* **2010**, *10*, 3209–3215. [CrossRef] [PubMed]
124. Turchanin, A.; Beyer, A.; Nottbohm, C.T.; Zhang, X.; Stosch, R.; Sologubenko, A.; Mayer, J.; Hinze, P.; Weimann, T.; Gölzhäuser, A. One nanometer thin carbon nanosheets with tunable conductivity and stiffness. *Adv. Mater.* **2009**, *21*, 1233–1237. [CrossRef]
125. Bertolazzi, S.; Brivio, J.; Kis, A. Stretching and breaking of ultrathin MoS_2. *ACS Nano* **2011**, *5*, 9703–9709. [CrossRef] [PubMed]

126. Klimov, N.N.; Jung, S.; Zhu, S.; Li, T.; Wright, C.A.; Solares, S.D.; Newell, D.B.; Zhitenev, N.B.; Stroscio, J.A. Electromechanical properties of graphene drumheads. *Science* **2012**, *336*, 1557–1561. [CrossRef] [PubMed]
127. Xu, P.; Neek-Amal, M.; Barber, S.D.; Schoelz, J.K.; Ackerman, M.L.; Thibado, P.M.; Sadeghi, A.; Peeters, F.M. Unusual ultra-low-frequency fluctuations in freestanding graphene. *Nat. Commun.* **2014**, *5*, 3720. [CrossRef] [PubMed]
128. Elibol, K.; Bayer, B.C.; Hummel, S.; Kotakoski, J.; Argentero, G.; Meyer, J.C. Visualising the strain distribution in suspended two-dimensional materials under local deformation. *Sci. Rep.* **2016**, *6*, 28485. [CrossRef] [PubMed]
129. He, X.; Tang, N.; Sun, X.; Gan, L.; Ke, F.; Wang, T.; Xu, F.; Wang, X.; Yang, X.; Ge, W.; et al. Tuning the graphene work function by uniaxial strain. *Appl. Phys. Lett.* **2015**, *106*, 043106. [CrossRef]
130. Manzeli, S.; Allain, A.; Ghadimi, A.; Kis, A. Piezoresistivity and strain-induced band gap tuning in atomically thin MoS_2. *Nano Lett.* **2015**, *15*, 5330–5335. [CrossRef] [PubMed]
131. Kim, S.K.; Bhatia, R.; Kim, T.-H.; Seol, D.; Kim, J.H.; Kim, H.; Seung, W.; Kim, Y.; Lee, Y.H.; Kim, S.-W. Directional dependent piezoelectric effect in cvd grown monolayer MoS_2 for flexible piezoelectric nanogenerators. *Nano Energy* **2016**, *22*, 483–489. [CrossRef]
132. Christman, J.A., Jr.; Woolcott, R.R., Jr.; Kingon, A.I.; Nemanich, R.J. Piezoelectric measurements with atomic force microscopy. *Appl. Phys. Lett.* **1998**, *73*, 3851–3853. [CrossRef]
133. Güthner, P.; Dransfeld, K. Local poling of ferroelectric polymers by scanning force microscopy. *Appl. Phys. Lett.* **1992**, *61*, 1137–1139. [CrossRef]
134. Kalinin, S.V.; Bonnell, D.A. Imaging mechanism of piezoresponse force microscopy of ferroelectric surfaces. *Phys. Rev. B* **2002**, *65*, 125408. [CrossRef]
135. Da Cunha Rodrigues, G.; Zelenovskiy, P.; Romanyuk, K.; Luchkin, S.; Kopelevich, Y.; Kholkin, A. Strong piezoelectricity in single-layer graphene deposited on SiO_2 grating substrates. *Nat. Commun.* **2015**, *6*, 7572. [CrossRef] [PubMed]
136. Zelisko, M.; Hanlumyuang, Y.; Yang, S.; Liu, Y.; Lei, C.; Li, J.; Ajayan, P.M.; Sharma, P. Anomalous piezoelectricity in two-dimensional graphene nitride nanosheets. *Nat. Commun.* **2014**, *5*, 4284. [CrossRef] [PubMed]
137. Bunch, J.S.; van der Zande, A.M.; Verbridge, S.S.; Frank, I.W.; Tanenbaum, D.M.; Parpia, J.M.; Craighead, H.G.; McEuen, P.L. Electromechanical resonators from graphene sheets. *Science* **2007**, *315*, 490–493. [CrossRef] [PubMed]
138. Chen, C.; Lee, S.; Deshpande, V.V.; Lee, G.-H.; Lekas, M.; Shepard, K.; Hone, J. Graphene mechanical oscillators with tunable frequency. *Nat. Nanotechnol.* **2013**, *8*, 923–927. [CrossRef] [PubMed]
139. Wu, W.; Wang, Z.L. Piezotronics and piezo-phototronics for adaptive electronics and optoelectronics. *Nat. Rev. Mater.* **2016**, *1*, 16031. [CrossRef]